Propagation of Spin Waves in Intersecting Yttrium Iron Garnet Nanowaveguides

D. Raskhodchikov,[1,†] J. Bensmann,[1,†] K.O. Nikolaev,[2,†] E. Lomonte,[1] L. Jin,[1] P. Steeger,[1] J.A. Preuß,[1] R. Schmidt,[1] R. Schneider,[1] J. Kern,[1] S. Michaelis de Vasconcellos,[1] R. Bratschitsch,[1] S.O. Demokritov,[2] W.H.P. Pernice,[1,3] and V.E. Demidov[2,*]

[1] *Institute of Physics, Center for Nanotechnology and Center for Soft Nanoscience, University of Muenster, 48149 Muenster, Germany*

[2] *Institute of Applied Physics, University of Muenster, 48149 Muenster, Germany*

[3] *Kirchhoff-Institute for Physics, Heidelberg University, 69120 Heidelberg, Germany*

(Received 26 July 2022; accepted 28 September 2022; published 28 November 2022)

We study experimentally the propagation of spin waves in waveguide structures consisting of two submicrometer-width yttrium iron garnet waveguides intersecting at a right angle. We show that, despite the significant spatial variations of the internal static magnet field and the in-plane anisotropy of the dispersion characteristics, the incident spin wave can efficiently pass through the microscopic cross-shaped structure and be transmitted into all its arms. This process depends strongly on the frequency of the wave and the orientation of the static magnetic field. By varying these parameters, one can achieve a controllable uniform or preferential transmission of the wave into different arms of the cross. Our results create the basis for the implementation of nanoscale magnonic networks to be used for the realization of complex non-Boolean data-processing schemes, including neuromorphic computing.

DOI: 10.1103/PhysRevApplied.18.054081

I. INTRODUCTION

In recent years, it has been shown that spin waves propagating in magnetic guiding structures provide a wide range of possibilities for the implementation of advanced nanoscale devices [1–6], including networks for non-Boolean data processing [7–10] and neuromorphic computing circuits [11–13]. These developments have been greatly advanced by the recent advent of high-quality ultrathin films of the magnetic insulator yttrium iron garnet (YIG) [14–16], which enabled efficient miniaturization of magnonic devices [17–20]. Due to the extremely low magnetic damping in this material, one can now achieve long-range propagation of spin waves [21,22] in microscopic magnonic structures with decay lengths significantly exceeding those in structures based on metallic ferromagnets [23]. Additionally, the propagation characteristics of spin waves in ultrathin YIG can be efficiently enhanced by using spin-transfer-torque effects [24,25].

The propagation of spin waves over long distances without the need for amplification and regeneration potentially enables extended magnonic circuits and networks consisting of a large number of individual devices to be built without the need to convert spin waves into conventional electronic signals and back, which drastically reduces the total losses of the entire circuit. Additionally, small spatial attenuation makes it possible to efficiently use nonlinear spin-wave phenomena that require large amplitudes of spin waves [4,26–28], which is particularly important for the implementation of neuromorphic architectures where nonlinearity plays a decisive role [11–13].

The development of complex magnonic networks requires a deep understanding of spin-wave propagation not only in simple straight spin-wave guides, but also in their junctions and crossings. In recent years, such devices have been studied for the case of metallic ferromagnetic materials and/or macroscopic dimensions [29–39], while nanopatterned YIG structures remain practically unexplored. Generally, such structures are expected to exhibit very specific spin-wave transmissions due to the relatively small width-to-thickness ratio typical for YIG nanowaveguides and the strong quantization of the spin-wave dispersion spectrum caused by small lateral dimensions. In particular, finite-size effects lead to a strong spatial variation of the static magnetic field, resulting in a tunnelinglike transmission of spin waves [40]. Additionally, the in-plane anisotropy of the strongly quantized dispersion spectrum is expected to significantly alter the transmission through the structures, where the wave vector changes its orientation with respect to the direction of the static magnetization.

Here, we use microfocus Brillouin-light-scattering (BLS) spectroscopy [23] to directly visualize the

*demidov@uni-muenster.de

†These authors contributed equally to this work.

propagation and transformation of spin waves in a magnetic cross composed of two 800-nm-wide YIG waveguides intersecting at a right angle. We show that, depending on the frequency, spin waves can experience predominant reflection from the intersection region with weak tunneling of the wave in the forward direction, an efficient redirection of the wave into the side arms of the cross, or almost uniform splitting of the wave into all three arms. Additionally, we find that the rotation of the direction of the static magnetic field results in suppression of the wave redirection into the side arms and leads to a strong increase in the forward transmission. These observations are in qualitative agreement with the results of micromagnetic simulations, which indicate that the reason for suppressed redirection lies in the peculiarities of the phase profiles of spin waves. The observed phenomena can be used to steer propagation of spin waves in complex nanoscale magnonic networks for the realization of advanced data processing.

II. EXPERIMENT

Figure 1 shows the schematics of the experiment. The studied waveguide structures are patterned from a 120-nm-thick YIG film by electron-beam lithography and argon-ion milling. The film grown by liquid-phase epitaxy is characterized by saturation magnetization, $4\pi M_s = 1750$ G, and a Gilbert damping parameter, $\alpha = 2 \times 10^{-4}$. The studied structures consist of two 800-nm-wide stripe waveguides (marked in Fig. 1 as WG1 and WG2) intersecting at a right angle. Spin waves are excited in waveguide WG1 using a 150-nm-thick and 500-nm-wide Au antenna, oriented perpendicular to the waveguide axis and located at a distance of 5 μm from the intersection. The excited spin waves with a frequency, f, determined by the frequency of the microwave current flowing through the antenna, propagate towards the intersection and split into the arms of the cross. The structure is magnetized by the static magnetic field, H_0, applied in the sample plane at an angle, φ, relative to the axis of the antenna.

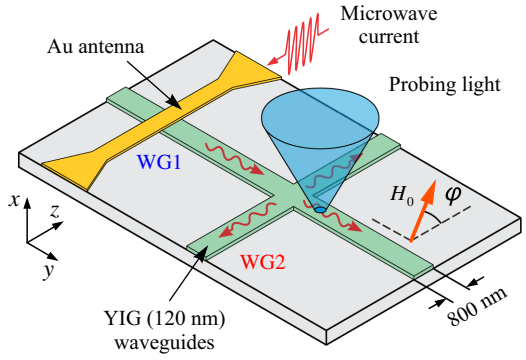

FIG. 1. Schematics of the experiment. Studied structures consist of two 800-nm-wide and 120-nm-thick YIG stripe waveguides (marked as WG1 and WG2) intersecting at a right angle. Spin waves are excited in waveguide WG1 using a 150-nm-thick and 500-nm-wide Au antenna, located at a distance of 5 μm from the intersection. Structure is magnetized by the static magnetic field, H_0, applied in the sample plane at angle φ relative to the axis of the antenna. Propagation of spin waves is visualized using microfocus BLS spectroscopy.

We study the propagation of waves with high spatial resolution using microfocus BLS spectroscopy [23]. This technique yields a signal that is proportional to the intensity of the spin waves at the position where the probing light is focused (Fig. 1). The probing light generated by a single-frequency laser has a wavelength of 473 nm and a power of 0.25 mW and is focused by a microscope objective lens with a magnification of 100 and a numerical aperture of 0.9 into a diffraction-limited spot. By moving the focal spot relative to the sample surface, we directly visualize the propagation of spin waves and determine the frequency- and field-dependent transmission of spin waves into the arms of the cross structure.

III. RESULTS AND DISCUSSION

Figures 2(a)–2(d) show representative spatial maps of the spin-wave intensity recorded at different excitation frequencies and the static magnetic field, $H_0 = 1.0$ kOe, oriented at an angle, $\varphi = 0$, as indicated. The maps are obtained by scanning the probing spot over an area of 8×8 μm^2 with a step size of 200 nm. The maps show that the character of the propagation of waves changes drastically when the excitation frequency is varied. At low frequencies [Fig. 2(a)], the wave is almost completely reflected from the intersection of the waveguides with the formation of a standing wave, the intensity of which vanishes near the intersection region. As the frequency increases [Fig. 2(b)], the spatial period of the standing wave decreases and nonzero transmission in the forward direction is observed, while transmission in the side arms remains negligible. Starting from a certain frequency [Fig. 2(c)], we additionally observe the propagation of waves into the side arms, and the intensity of the waves transmitted into all three arms becomes approximately equal. Finally, as the frequency is increased further, the transmission in the forward direction becomes weaker again, and the propagation process becomes dominated by the redirection of the waves into the side arms. These behaviors are characterized quantitatively in Fig. 2(e), which shows the frequency dependence of the transmission coefficients T_{12} and T_{13}, which are defined as the ratio of the BLS intensities detected at spatial points $P1$–$P3$ located in different arms of the cross at a distance of 1 μm from the center of the intersection region [see Fig. 2(a)]. The coefficient T_{12}, which characterizes the transmission in the forward direction ($P1$ to $P2$), remains below 5% at low frequencies, shows an abrupt increase at $f \approx 4.3$ GHz,

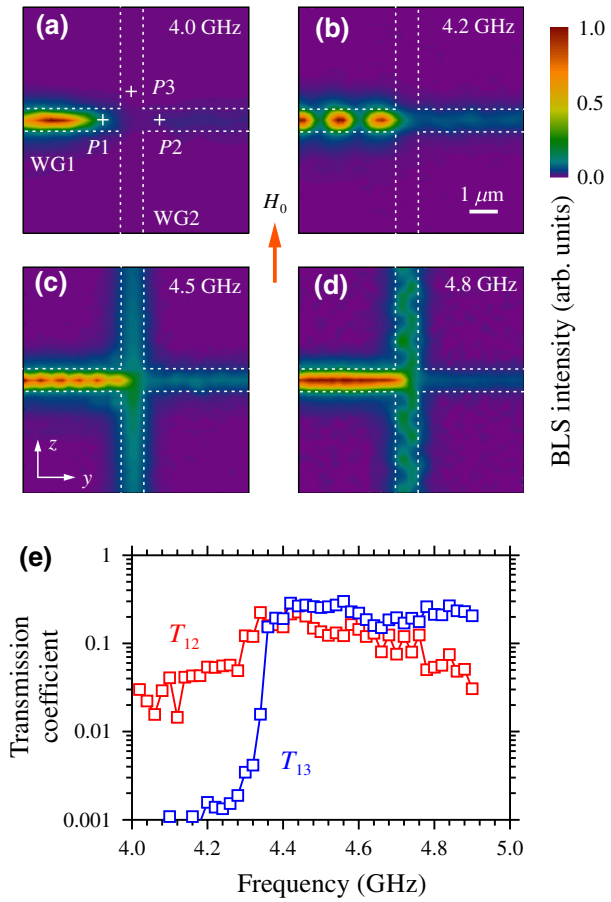

FIG. 2. (a)–(d) Representative spatial maps of spin-wave intensity recorded at different excitation frequencies, as labeled. (e) Frequency dependence of transmission coefficients T_{12} and T_{13} defined as the ratio of the intensities of the waves detected at spatial points $P1$–$P3$ located in different arms of the cross, as shown in (a). Data are obtained at $H_0 = 1.0$ kOe and $\varphi = 0$.

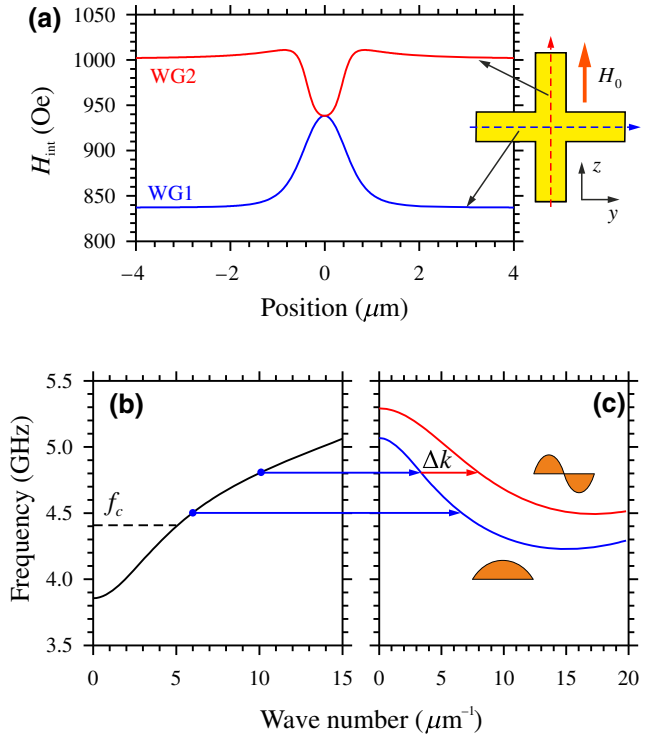

FIG. 3. (a) Calculated spatial profiles of the internal static magnetic field, H_{int}, along the axes of the two waveguides, as shown in the inset. (b),(c) Calculated dispersion curves of spin waves in WG1 and WG2 (solid curves). Horizontal dashed line in (b) marks the estimated cutoff frequency, f_c, of the DE waves in the intersection region. Insets in (c) schematically illustrate the distributions of the dynamic magnetization in the transverse section of the waveguide corresponding to the shown BV modes. Arrows illustrate the transformation of DE waves in WG1 into BV waves in WG2. Data are obtained at $H_0 = 1.0$ kOe and $\varphi = 0$.

reaching a maximum value of about 20% at $f = 4.34$ GHz, and then gradually decreases back to 3%–5% at higher frequencies (note the logarithmic scale of the vertical axis). The coefficient T_{13}, which characterizes the redirection of waves into the side arms ($P1$ to $P3$), is negligibly small at low frequencies, increases abruptly at $f \approx 4.3$ GHz, and then remains approximately constant [$(\approx 20 \pm 5)\%$] in the rest of the studied frequency range.

To gain an insight into the observed behaviors, we analyze the spatial distributions of the internal static magnetic field, H_{int}, and the dispersion spectra of spin waves in the waveguides. Figure 3(a) shows the profiles of H_{int} along the axes of the two waveguides calculated using the micromagnetic simulation package mumax3 [41] for $H_0 = 1.0$ kOe and $\varphi = 0$. In these calculations, we consider a computation domain with dimensions of $12\,000 \times 12\,000 \times 120$ nm^3 discretized into $10 \times 10 \times 10$ nm^3 cells. The standard value for the YIG exchange constant of $A = 3.66 \times 10^{-7}$ erg/cm is used. All the other parameters are set in accordance with the values known from the experiment. Since the external field, H_0, is oriented perpendicular to WG1, H_{int} in this waveguide is reduced to 0.84 kOe due to demagnetization effects [23]. In contrast, $H_{\text{int}} \approx H_0$ in WG2, which is magnetized parallel to its axis. In the intersection region, H_{int} takes an intermediate value of 0.93 kOe, which corresponds to a local increase of the field in WG1 and a local decrease of the field in WG2.

Figures 3(b) and 3(c) show the dispersion spectra of spin waves for WG1 and WG2, respectively, calculated using analytical theory [42] and the approach described in Ref. [43]. In the used magnetization configuration, the waves excited in WG1 are of the Damon-Eshbach (DE) type [44]. Their frequency increases with increasing wave number, starting from the lower cutoff frequency of about 3.9 GHz [Fig. 3(b)]. To pass through the cross along WG1 in the forward direction, these waves have to propagate through the region of increased internal field [Fig. 3(a)], where the cutoff frequency locally increases.

Because the width of the waveguide is not constant in this region, the local cutoff frequency cannot be calculated exactly. As a coarse estimate, we use the frequency of the ferromagnetic resonance, $f_c = 4.4$ GHz, obtained for $H_{\text{int}} = 0.93$ kOe [horizontal dashed line in Fig. 3(b)]. For frequencies $f < f_c$, there are no allowed spectral states in the intersection region. Therefore, waves at low frequencies are transmitted through the cross in the tunneling regime [40], which results in small values of the transmission coefficient, T_{12} [Fig. 2(e)]. In this regime, the increase in the frequency towards f_c leads to a gradual increase in T_{12} due to a decrease in the effective height of the tunneling barrier. As the frequency is increased above 4.3 GHz, which agrees reasonably well with the calculated f_c, T_{12} rises abruptly [Fig. 2(e)], indicating a transition to a normal propagation regime. We emphasize that, even in this regime, the local increase in H_{int} in the intersection region leads to partial reflection of waves, and T_{12} remains limited to 20%–25%. According to data in Fig. 2(e), these reflections become stronger with increasing frequency (decreasing wavelength) of spin waves. Note that, in the studied microscopic structures, the spatial extent of the inhomogeneity of H_{int} in the intersection region is comparable to the wavelength of the incident spin wave. Therefore, the reflection and transmission of spin waves through this inhomogeneity is a nonadiabatic process strongly influenced by long-range dynamic dipolar fields of the wave. Since the field of a wave with a longer wavelength extends to a longer distance, one expects better transmission through the inhomogeneity at lower frequencies.

The redirection of waves into the side arms can be considered as a conversion of the DE waves in WG1 into backward-volume (BV) waves in WG2. The dispersion spectrum of these waves is shown in Fig. 3(c) for the two lowest-order transverse modes of the waveguide characterized by a symmetric and antisymmetric distribution of the dynamic magnetization across the waveguide width, as schematically shown in the insets in Fig. 3(c). As seen from these data, BV waves possess the lowest frequency of about 4.2 GHz at a relatively large wave number, corresponding to a wavelength of about 400 nm. In agreement with these data, T_{13} becomes nonzero at 4.2 GHz [Fig. 2(e)]. However, at these frequencies, T_{13} is very small. As the frequency increases above 4.2 GHz, the wavelength quickly increases [Fig. 3(c)], which results in the increase of the excitation efficiency and a rapid increase in T_{13}.

We note that, in the frequency range of 4.2–4.3 GHz, the redirection of spin waves into the side arms is accompanied by a strong decrease in the wavelength and the group velocity. Due to the reduced sensitivity of the BLS apparatus to spin waves with short wavelengths, the values of T_{13} obtained from BLS measurements in the frequency range of 4.2–4.3 GHz are smaller than the actual values [45]. Additionally, due to a strong variation of the group velocity in this range, the intensity of waves in the side arms is expected to increase to fulfill the condition of conservation of the energy flux [46].

It is important to note that, at frequencies above 4.5 GHz, the excited BV wave exhibits a snakelike intensity pattern [Fig. 2(d)], which is associated with the simultaneous excitation of the symmetric and antisymmetric waveguide modes [23], as shown by the arrows in Figs. 3(b) and 3(c). As seen from the maps recorded at $f = 4.6$–4.9 GHz [Fig. 4(a)], the spatial period of the pattern noticeably increases with increasing frequency. This period is determined by the difference in the wave numbers of the modes, Δk [Fig. 3(c)], and can be calculated as $L = 2\pi/\Delta k$. Figure 4(b) shows the frequency dependence of the spatial period obtained from the Fourier analysis of the measured maps (symbols) together with the dependence obtained from the analysis of the calculated dispersion spectra (solid curve). As seen from Fig. 4(b), experimental data are in excellent agreement with the prediction from theory, which demonstrates the validity of the analysis.

We now turn to the effects of the orientation of the static magnetic field. Figures 5(a)–5(d) show the spin-wave intensity maps recorded at $f = 4.5$ GHz for angle φ

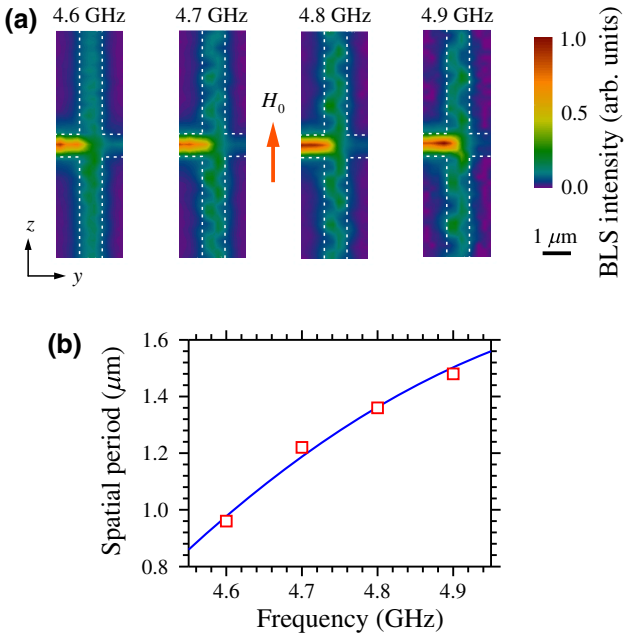

FIG. 4. (a) Spatial maps of the spin-wave intensity recorded at different excitation frequencies, as labeled. (b) Frequency dependence of the spatial period of the snakelike pattern obtained from the Fourier analysis of the measured maps (symbols) together with the dependence obtained from the analysis of the calculated dispersion spectra (solid curve). Data are obtained at $H_0 = 1.0$ kOe and $\varphi = 0$.

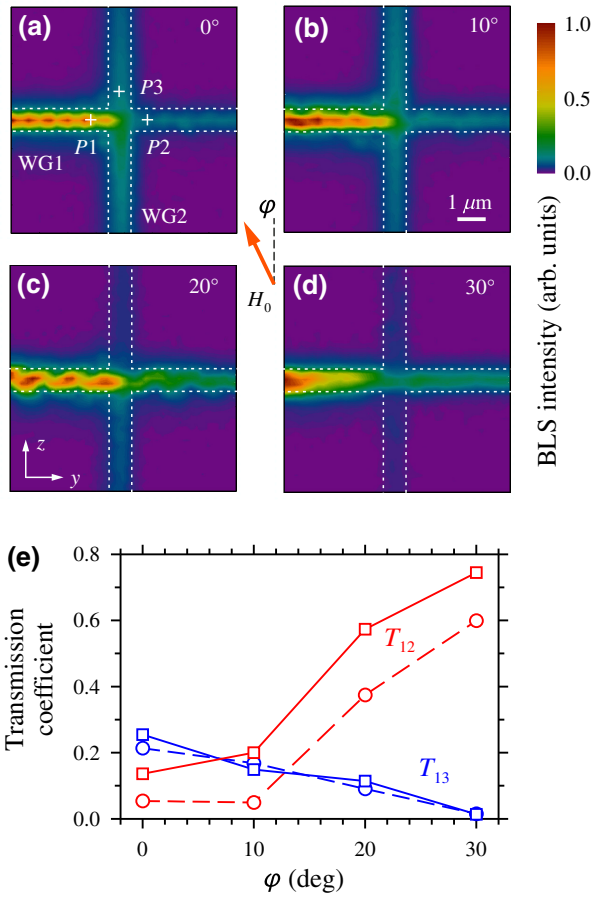

FIG. 5. (a)–(d) Spatial maps of the spin-wave intensity recorded at different angles of the static magnetic field, φ, as labeled. Data are obtained at $H_0 = 1.0$ kOe and $f = 4.5$ GHz. (e) Angular dependence of the transmission coefficients T_{12} and T_{13}. Squares and solid lines show data obtained at $f = 4.5$ GHz. Circles and dashed lines show data obtained at $f = 4.8$ GHz.

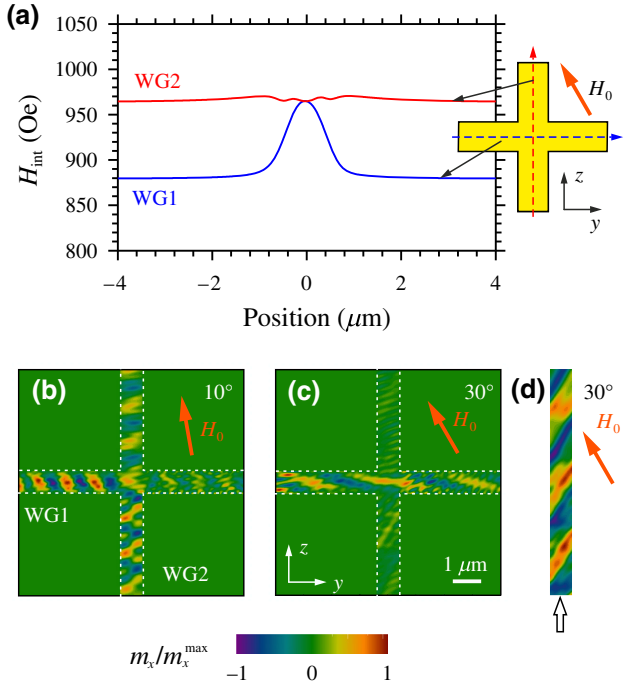

FIG. 6. (a) Calculated spatial profiles of the internal static magnetic field, H_{int}, along the axes of the two waveguides, as shown in the inset. Calculations are performed at $H_0 = 1.0$ kOe and $\varphi = 30°$. (b)–(d) Snapshots of the normalized out-of-plane magnetization component obtained from micromagnetic simulations of spin-wave propagation. Spin waves are excited by applying a localized dynamic magnetic field with a frequency of 4.5 GHz. (b),(c) Complete cross structure magnetized at $\varphi = 10$ and 30°, respectively. (d) Single waveguide magnetized at $\varphi = 30°$.

increasing from 0 to 30°, and Fig. 5(e) shows the angular dependences of the transmission coefficients T_{12} and T_{13}. These data reveal a clear tendency of the increase in transmission in the forward direction (T_{12}) with simultaneous suppression of the redirection of waves into the side arms (T_{13}).

To understand the above findings, we consider the spatial profiles of H_{int} calculated for $\varphi = 30°$ [Fig. 6(a)]. As seen from these data, the height of the potential barrier for waves propagating in the forward direction becomes noticeably smaller at increased angles [compare with Fig. 3(a)]. This fact can explain the observed increase in the forward transmission. However, the profiles of the field cannot explain the reduction of the transmission into the side arms. Indeed, the profile of H_{int} in WG2 becomes much more uniform in comparison to the case of $\varphi = 0$, which can only improve the coupling of the DE and BV waves, in contrast to the experimental observations.

To clarify the reason for this behavior, we perform micromagnetic simulations of spin-wave propagation in the cross structure magnetized at different angles. In these simulations, we excite spin waves by applying an x-polarized dynamic magnetic field with a frequency of 4.5 GHz and an amplitude of 0.1 Oe in a 500-nm-wide region located at a distance of 5 μm from the intersection of the waveguides, which models the antenna used in the experiment. To avoid spin-wave reflections from the boundaries of the computation domain, the damping parameter is exponentially increased close to its edges.

Figures 6(b) and 6(c) show the maps of the normalized out-of-plane magnetization component obtained for $f = 4.5$ GHz and $\varphi = 10$ and 30°, respectively. Note that, in contrast to the experimental intensity maps, the maps in Figs. 6(b) and 6(c) are snapshots of dynamic magnetization, which contain important information about the phase of spin waves. Comparing data obtained for the two angles, one clearly sees that the simulations reproduce the experimentally observed enhancement of the transmission in the forward direction and suppression of the transmission into

the side arms. In full agreement with the experiment, the latter transmission almost completely vanishes at $\varphi = 30°$.

The lack of transmission in the side arms could be caused by the shift of the dispersion spectra of spin waves in WG1 and WG2 due to the variation of the internal magnetic field in these waveguides, which can potentially lead to the absence of spectral states in WG2 at $f = 4.5$ GHz for $\varphi = 30°$. To verify this assumption, we consider the direct excitation of spin waves in a single waveguide oriented in the z direction (WG2) by a localized dynamic magnetic field at $f = 4.5$ GHz. The results of these calculations [Fig. 6(d)] indicate that WG2 supports the propagation of waves at this frequency and that the waves possess a moderate wavelength of about 2 μm. This leads us to the conclusion that, although waves at this frequency can propagate in both waveguides, they cannot efficiently couple to each other in the intersection region. This weak coupling can be caused by the peculiarities of the spatial structure of the phase of spin waves. As seen from Figs. 6(b) and 6(c), the phase fronts progressively tilt as the angle φ increases. This results in a progressively increasing mismatch in the phase structure of the waves in WG1 and WG2, hindering their mutual conversion.

IV. CONCLUSIONS

Here, we show that the propagation of spin waves in intersecting microscopic YIG waveguides is not trivial and can be efficiently controlled by varying the frequency and direction of static magnetization. This controllability is useful for steering the propagation of spin waves in complex nanoscale magnonic networks for the implementation of nontraditional computing and signal processing. The high sensitivity of the propagation regime to the frequency of spin waves provides additional opportunities for the manipulation of spin-wave propagation by nonlinear effects, such as an amplitude-dependent shift of the spin-wave spectrum. This opportunity is particularly important for the realization of neuromorphic networks, where the nonlinear response plays a key role.

ACKNOWLEDGMENTS

This work is supported by the Deutsche Forschungsgemeinschaft (DFG, German Research Foundation) Project No. 433682494–SFB 1459.

[1] S. Dutta, S.-C. Chang, N. Kani, D. E. Nikonov, S. Manipatruni, I. A. Young, and A. Naeemi, Non-volatile clocked spin wave interconnect for beyond-CMOS nanomagnet pipelines, Sci. Rep. **5**, 9861 (2015).

[2] G. Csaba, A. Papp, and W. Porod, Perspectives of using spin waves for computing and signal processing, Phys. Lett. A **381**, 1471 (2017).

[3] A. Mahmoud, F. Ciubotaru, F. Vanderveken, A. V. Chumak, S. Hamdioui, C. Adelmann, and S. Cotofana, Introduction to spin wave computing, J. Appl. Phys. **128**, 161101 (2020).

[4] Q. Wang, M. Kewenig, M. Schneider, R. Verba, F. Kohl, B. Heinz, M. Geilen, M. Mohseni, B. Lägel, F. Ciubotaru, et al., A magnonic directional coupler for integrated magnonic half-adders, Nat. Electr. **3**, 765 (2020).

[5] H. Qin, R. B. Holländer, L. Flajšman, F. Hermann, R. Dreyer, G. Woltersdorf, and S. van Dijken, Nanoscale magnonic Fabry-Perot resonator for low-loss spin-wave manipulation, Nat. Commun. **12**, 2293 (2021).

[6] J. Chen, H. Wang, T. Hula, C. Liu, S. Liu, T. Liu, H. Jia, Q. Song, C. Guo, Y. Zhang, *et al.*, Reconfigurable spin-wave interferometer at the nanoscale, Nano Lett. **21**, 6237 (2021).

[7] F. Gertz, A. Kozhevnikov, Y. Filimonov, and A. Khitun, Magnonic holographic memory, IEEE Trans. Magn. **51**, 4002905 (2015).

[8] A. Kozhevnikov, F. Gertz, G. Dudko, Y. Filimonov, and A. Khitun, Pattern recognition with magnonic holographic memory device, Appl. Phys. Lett. **106**, 142409 (2015).

[9] Y. Khivintsev, M. Ranjbar, D. Gutierrez, H. Chiang, A. Kozhevnikov, Y. Filimonov, and A. Khitun, Prime factorization using magnonic holographic devices, J. Appl. Phys. **120**, 123901 (2016).

[10] Y. V. Khivintsev, V. K. Sakharov, A. V. Kozhevnikov, G. M. Dudko, Y. A. Filimonov, and A. Khitun, Spin waves in YIG based magnonic networks: Design and technological aspects, J. Magn. Magn. Mater. **545**, 168754 (2022).

[11] M. Zahedinejad, A. A. Awad, S. Muralidhar, R. Khymyn, H. Fulara, H. Mazraati, M. Dvornik, and J. Åkerman, Two-dimensional mutually synchronized spin Hall nano-oscillator arrays for neuromorphic computing, Nat. Nanotech. **15**, 47 (2020).

[12] A. Papp, G. Csaba, and W. Porod, Characterization of nonlinear spin-wave interference by reservoir-computing metrics, Sci. Rep. **11**, 14239 (2021).

[13] A. Papp, W. Porod, and G. Csaba, Nanoscale neural network using non-linear spin-wave interference, Nat. Commun. **12**, 6244 (2021).

[14] Y. Sun, Y. Y. Song, H. Chang, M. Kabatek, M. Jantz, W. Schneider, M. Wu, H. Schultheiss, and A. Hoffmann, Growth and ferromagnetic resonance properties of nanometer-thick yttrium iron garnet films, Appl. Phys. Lett. **101**, 152405 (2012).

[15] O. d'Allivy Kelly, A. Anane, R. Bernard, J. Ben Youssef, C. Hahn, A. H. Molpeceres, C. Carretero, E. Jacquet, C. Deranlot, P. Bortolotti, *et al.*, Inverse spin Hall effect in nanometer-thick yttrium iron garnet/Pt system, Appl. Phys. Lett. **103**, 082408 (2013).

[16] C. Hauser, T. Richter, N. Homonnay, C. Eisenschmidt, M. Qaid, H. Deniz, D. Hesse, M. Sawicki, S. G. Ebbinghaus, and G. Schmidt, Yttrium iron garnet thin films with very low damping obtained by recrystallization of amorphous material, Sci. Rep. **6**, 20827 (2016).

[17] S. Li, W. Zhang, J. Ding, J. E. Pearson, V. Novosad, and A. Hoffmann, Epitaxial patterning of nanometer-thick $Y_3Fe_5O_{12}$ films with low magnetic damping, Nanoscale **8**, 388 (2016).

[18] Q. Wang, B. Heinz, R. Verba, M. Kewenig, P. Pirro, M. Schneider, T. Meyer, B. Lägel, C. Dubs, T. Brächer, and A. V. Chumak, Spin Pinning and Spin-Wave Dispersion

in Nanoscopic Ferromagnetic Waveguides, Phys. Rev. Lett. **122**, 247202 (2019).

[19] F. Heyroth, C. Hauser, P. Trempler, P. Geyer, F. Syrowatka, R. Dreyer, S. G. Ebbinghaus, G. Woltersdorf, and G. Schmidt, Monocrystalline Freestanding Three-Dimensional Yttrium-Iron-Garnet Magnon Nanoresonators, Phys. Rev. Appl. **12**, 054031 (2019).

[20] B. Heinz, T. Brächer, M. Schneider, Q. Wang, B. Lägel, A. M. Friedel, D. Breitbach, S. Steinert, T. Meyer, M. Kewenig, *et al.*, Propagation of spin-wave packets in individual nanosized yttrium iron garnet magnonic conduits, Nano Lett. **20**, 4220 (2020).

[21] H. Yu, O. d'Allivy Kelly, V. Cros, R. Bernard, P. Bortolotti, A. Anane, F. Brandl, F. Heimbach, and D. Grundler, Approaching soft x-ray wavelengths in nanomagnet-based microwave technology, Nat. Commun. **7**, 11255 (2016).

[22] C. Liu, *et al.*, Long-distance propagation of short-wavelength spin waves, Nat. Commun. **9**, 738 (2018).

[23] V. E. Demidov and S. O. Demokritov, Magnonic waveguides studied by micro-focus Brillouin light scattering, IEEE Trans. Magn. **51**, 0800215 (2015).

[24] M. Evelt, V. E. Demidov, V. Bessonov, S. O. Demokritov, J. L. Prieto, M. Munoz, J. Ben Youssef, V. V. Naletov, G. de Loubens, O. Klein, *et al.*, High-efficiency control of spin-wave propagation in ultra-thin yttrium iron garnet by the spin-orbit torque, Appl. Phys. Lett. **108**, 172406 (2016).

[25] M. Evelt, L. Soumah, A. B. Rinkevich, S. O. Demokritov, A. Anane, V. Cros, J. Ben Youssef, G. de Loubens, O. Klein, P. Bortolotti, and V. E. Demidov, Emission of Coherent Propagating Magnons by Insulator-Based Spin-Orbit-Torque Oscillators, Phys. Rev. Appl. **10**, 041002 (2018).

[26] A. Papp, M. Kiechle, S. Mendisch, V. Ahrens, L. Sahin, L. Seitner, W. Porod, G. Csaba, and M. Becherer, Experimental demonstration of a concave grating for spin waves in the Rowland arrangement, Sci. Rep. **11**, 14239 (2021).

[27] S. R. Lake, B. Divinskiy, G. Schmidt, S. O. Demokritov, and V. E. Demidov, Interplay between Nonlinear Spectral Shift and Nonlinear Damping of Spin Waves in Ultrathin Yttrium Iron Garnet Waveguides, Phys. Rev. Appl. **17**, 034010 (2022).

[28] H. Merbouche, B. Divinskiy, K. O. Nikolaev, C. Kaspar, W. H. P. Pernice, D. Gouéré, R. Lebrun, V. Cros, J. Ben Youssef, P. Bortolotti, *et al.*, Giant nonlinear self-phase modulation of large-amplitude spin waves in microscopic YIG waveguides, Sci. Rep. **12**, 7246 (2022).

[29] T. Brächer, P. Pirro, J. Westermann, T. Sebastian, B. Lägel, B. Van de Wiele, A. Vansteenkiste, and B. Hillebrands, Generation of propagating backward volume spin waves by phase-sensitive mode conversion in two-dimensional microstructures, Appl. Phys. Lett. **102**, 132411 (2013).

[30] K. Vogt, F. Y. Fradin, J. E. Pearson, T. Sebastian, S. D. Bader, B. Hillebrands, A. P. Hoffmann, and H. Schultheiss, Realization of a spin-wave multiplexer, Nat. Commun. **5**, 3727 (2014).

[31] K. Nanayakkara, A. Anferov, A. P. Jacob, S. J. Allen, and A. Kozhanov, Cross junction spin wave logic architecture, IEEE Trans. Magn. **50**, 3402204 (2014).

[32] K. Nanayakkara, A. P. Jacob, and A. Kozhanov, Spin wave scattering and interference in ferromagnetic cross, J. Appl. Phys. **118**, 163904 (2015).

[33] A. V. Sadovnikov, C. S. Davies, S. V. Grishin, V. V. Kruglyak, D. V. Romanenko, Y. P. Sharaevskii, and S. A. Nikitov, Magnonic beam splitter: The building block of parallel magnonic circuitry, Appl. Phys. Lett. **106**, 192406 (2015).

[34] C. S. Davies, A. Francis, A. V. Sadovnikov, S. V. Chertopalov, M. T. Bryan, S. V. Grishin, D. A. Allwood, Y. P. Sharaevskii, S. A. Nikitov, and V. V. Kruglyak, Towards graded-index magnonics: Steering spin waves in magnonic networks, Phys. Rev. B **92**, 020408 (2015).

[35] N. Kanazawa, T. Goto, K. Sekiguchi, A. B. Granovsky, C. A. Ross, H. Takagi, Y. Nakamura, H. Uchida, and M. Inoue, The role of Snell's law for a magnonic majority gate, Sci. Rep. **7**, 7898 (2017).

[36] H. J. J. Liu, A. Guerrero, K. E. Nygren, M. Swyt, and K. S. Buchanan, Spin wave wavevector up-conversion in Y-shaped Permalloy structures, Appl. Phys. Lett. **119**, 172403 (2021).

[37] T. Taniguchia and C. H. Back, Mode selective excitation of spin waves, Appl. Phys. Lett. **120**, 032402 (2022).

[38] M. Balinskiy, D. Gutierrez, H. Chiang, Y. Filimonov, A. Kozhevnikov, and A. Khitun, Spin wave interference in YIG cross junction, AIP Adv. **7**, 056633 (2017).

[39] M. Balynskiy, H. Chiang, A. Kozhevnikov, G. Dudko, Y. Filimonov, A. A. Balandin, and A. Khitun, Effects of the magnetic field variation on the spin wave interference in a magnetic cross junction, AIP Adv. **8**, 056619 (2018).

[40] S. O. Demokritov, A. A. Serga, A. Andre, V. E. Demidov, M. P. Kostylev, B. Hillebrands, and A. N. Slavin, Tunneling of Dipolar Spin Waves through a Region of Inhomogeneous Magnetic Field, Phys. Rev. Lett. **93**, 047201 (2004).

[41] A. Vansteenkiste, J. Leliaert, M. Dvornik, M. Helsen, F. Garcia-Sanchez, and B. Van Waeyenberge, The design and verification of MuMax3, AIP Adv. **4**, 107133 (2014).

[42] B. A. Kalinikos and A. N. Slavin, Theory of dipole-exchange spin wave spectrum for ferromagnetic films with mixed exchange boundary conditions, J. Phys. C: Solid State Phys. **19**, 7013 (1986).

[43] V. E. Demidov, S. O. Demokritov, K. Rott, P. Krzysteczko, and G. Reiss, Mode interference and periodic self-focusing of spin waves in permalloy microstripes, Phys. Rev. B **77**, 064406 (2008).

[44] R. W. Damon and J. R. Eshbach, Magnetostatic modes of a ferromagnetic slab, J. Phys. Chem. Solids **19**, 308 (1961).

[45] S. R. Lake, B. Divinskiy, G. Schmidt, S. O. Demokritov, and V. E. Demidov, Efficient geometrical control of spin waves in microscopic YIG waveguides, Appl. Phys. Lett. **119**, 182401 (2021).

[46] K. Baumgaertl, J. Gräfe, P. Che, A. Mucchietto, J. Förster, N. Träger, M. Bechtel, M. Weigand, G. Schütz, and D. Grundler, Nanoimaging of ultrashort magnon emission by ferromagnetic grating couplers at GHz frequencies, Nano Lett. **20**, 7281 (2020).